European Journal of Applied Physics
Vol 1 | Issue 1 | Month 2025
ISSN 2684-4451

RESEARCH ARTICLE

Analysis of Trigger Input for Nuclear Reactions Using SUS Alloys

Tadahiko Mizuno*

ABSTRACT

The authors tested various metals and alloys as reactants. Since 2020, we have investigated numerous phenomena that occur when a cylindrical container machined from a stainless-steel container is heated. Using this method, we have confirmed abnormal heat generation (thermal output - thermal input > 0), neutron generation, electromagnetic wave generation, and, when a collecting electrode is installed in the container, electromotive force generation. We analyzed the input power that triggers these phenomena and reported the results here.

Keywords: Electron generation, neutron generation, nuclear reaction, trigger reaction.

Submitted: Month 00, 2025
Published: Month 00, 2025

10.24018/ejphysics.2025.1.1.393

Hydrogen Engineering Development & Application Ltd., Japan Three System Building 6F, Japan.

****Corresponding Author:***
e-mail: mzn@n-head.com

1. Introduction

We reported that neutrons with an energy of 0.7 MeV were generated when SUS304 alloy was compressed and stretched and heated from 300°C to 800°C [1]. The author reported weak neutron generation during electrolysis in a heavy water solution as an anomalous phenomenon occurring in metal-hydrogen systems [2]. After electrolysis tests, the isotopic changes of elements precipitated in the electrolyte were analyzed [3]–[7]. Heat generation during these experiments was difficult to control. Heat generation from other metals has been reported in the Ni-H system [8]–[9]. The author placed Ni mesh as a reactant inside a stainless-steel container. The container was then heated to 800°C in an insulated thermal measurement box. This method obtained excess heat generation from the container (heat output - input > 0). In 2020, it was found that a cylindrically machined SUS304 container generated excess heat at high temperatures up to 800°C [10]. Tests at temperatures above this temperature were not performed due to safety and component heat resistance reasons.

2. Method

2.1. Reaction Container

The schematic diagram of the container used is shown in Fig. 1. A 3.2 mm thick SUS304 plate was subjected to bending stress to form a cylindrical shape. The diameter of the cylinder was 70–100 mm. The top and bottom of the figure are cross-sectional views of a typical plate and cylinder. The joining surfaces of the cylinder were TIG welded and polished. The inner surface was finally polished with a 400-mesh buff. The bending process applied tensile stress to the convex surface of the SUS material and compressive stress to the concave surface. Both surfaces transformed from austenite (face-centered cubic structure) to a phase containing martensite (body-centered cubic structure) [11].

Furthermore, defects and dislocations were generated in the SUS due to the bending stress. This is believed to form reaction sites within the curved SUS [12].

Fig. 2 shows the exterior of the cylindrical container. The container was made of SUS304 stainless steel alloy manufactured by Canon Anelva Corporation. SUS304 is known as AISI 304 in the United States. The inner surface is finally given a mirror-like gloss finish. Flanges made of ICF152 and SUS304 are attached to both ends. A vacuum exhaust tube with a diameter of 1/4 inch and a length of 100 mm is welded to the flange at one end. The entire container weighs 12.7 kg, and the tube itself has a diameter

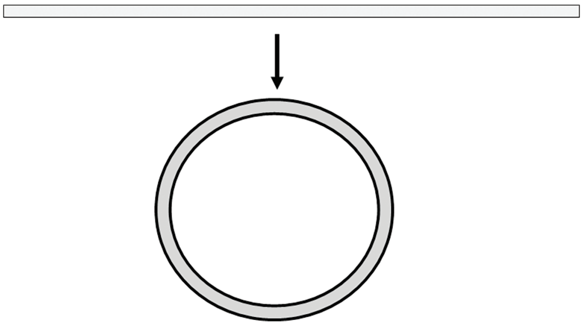

Fig. 1. Stainless steel sheet material (top) transformed into a cylindrical shape (bottom) by bending.

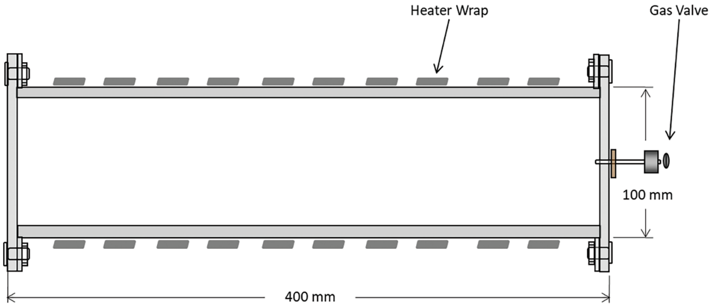

Fig. 2. Appearance of the container.

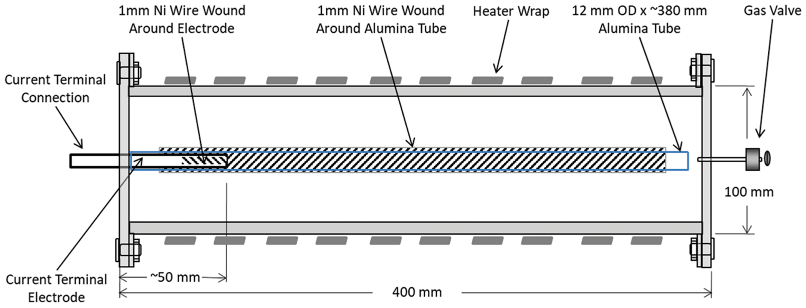

Fig. 3. Internal structure of the container.

of 100 mm and a length of 400 mm. A heater is wrapped around this cylindrical part. Details are explained in Fig. 5.

During processing, SUS304 contains austenite with an FCC structure and martensite with a BCC structure. The diffusion rate of hydrogen atoms in martensite is approximately six orders of magnitude faster than in austenite [13].

Austenite: Hydrogen atom diffusion rate 4×10^{-16} m^2/s

Martensite: Hydrogen atom diffusion rate 1.8×10^{-10} m^2/s

As shown in Fig. 3, a mini 100A current collecting electrode manufactured by Canon Anelva Corporation is attached to the center of the flange at the other end of the container, and a positive lead wire is connected to it. Inside the electrode container is a 50 mm long nickel-plated copper terminal, to which an alumina pipe (inner diameter 9 mm, outer diameter 13 mm, length 300 mm) is attached, and nickel wire (diameter 1 mm, length 100 mm) is wound around it and connected to the main body of the electrode. The voltage between the output at the center of the electrode and ground is directly input into a data logger. The center of the electrode is insulated and not electrically connected to the outer container.

A photograph of the test container is shown in Fig. 4. It weighs 6 kg.

Fig. 5 shows a photograph of the heater wrapped around the container. The heater (Sanko Electric Industry Co., Ltd., 101G, 2.3 × 3300, 100 V 600 W, heat-resistant to 800°C) is wrapped around the outer circumference of the container approximately 10 times. After evacuating the container, it is filled with 500 Pa of hydrogen gas and left for 60 minutes to saturate the gas. The container is then evacuated to a few Pa. Finally, before heating the container, it is confirmed that there are no air leaks and that the pressure inside the container remains constant. It weighs 6.2 kg. With flanges attached on both ends, the weight is 12.7 kg.

Fig. 4. Photograph of SUS test furnace.

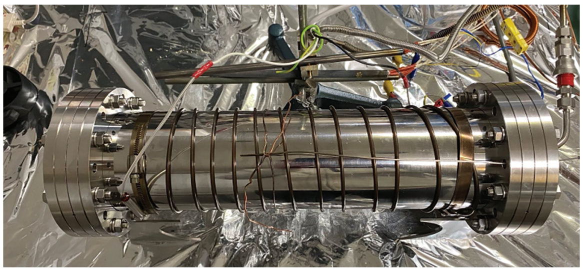

Fig. 5. Photograph of a heater wrapped around SUS container.

Fig. 6. Container covered with insulating material.

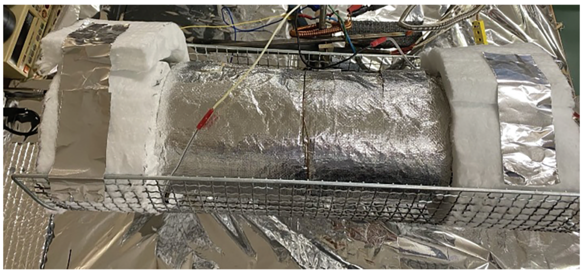

Fig. 7. The entire container was covered with insulation to ensure a uniform temperature.

Fig. 6 shows a photo of a heater wrapped in a 2 cm thick rock wool insulation. The surface is covered with 0.3 mm thick aluminum foil to reflect heat from the inside. The weight is 13.5 kg.

Fig. 7 shows how the metal parts on both ends of the container are completely covered with rock wool to prevent heat from escaping. This is to keep the container temperature uniform. The container weighs 14 kg.

2.2. *Heat Measurement Method*

Fig. 8 shows a schematic of a calorimetric heat measurement box. Air enters from the center of the right side of the figure and exits from the center of the left side. Air temperature is measured at both the inlet and outlet. The inside of the box is insulated from the other box on all four sides with rock wool. The container is placed inside the calorimetric measurement box, with hard wool placed at the bottom and soft wool surrounding the container, which is then surrounded by hard wool again. Heat transfer, heat radiation, and convection from the reaction container are all captured by the rock wool and transferred to the air.

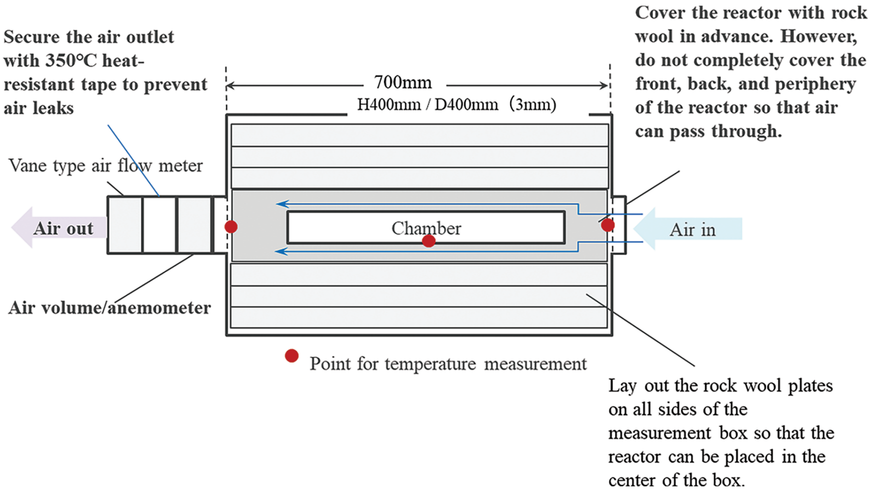

Fig. 8. Schematic of the inside of the thermal test box.

2.3. *Calorific Value Calculation Method*

The heat measurement calculation is as follows. The constant pressure specific heat of air, C_p, is almost unaffected by temperature, but is approximately expressed by Eq. (1). In a typical measurement, when the room temperature was 293 K, the maximum temperature at the air outlet was 390 K. In this case, the heat capacity of the heated air increased by 3%. Tout is the air outlet temperature. These temperatures are measured continuously at both the air inlet and outlet, but the effect of the temperature coefficient on the heat capacity can be assumed to be negligible, being less than 1/10 of the temperature measurement error.

$$C_p = 0.987 + 0.0000661 \times T_{out} \tag{1}$$

The input, Win, is calculated using Eq. (2).

$$W_{in} = \sum_0^T \Delta W \times \ \Delta t = \int_0^T (Wt)\, dt \tag{2}$$

Here, ΔW is the power supplied during the measurement period (5 seconds in this test), and Δt is the data collection interval (5 seconds). The output power H_{out} is calculated using Eq. (3).

$$H_{out} = \sum_0^T \Delta V \times Cp \times \Delta t = \int_0^T dV \times Cp \times dTdt \tag{3}$$

For the output power H_{out}, V is the airflow rate (m^3/s). Since the heat recovery rate of the measurement system is approximately 1, there is no need to consider heat loss. Therefore, the equation is simply "airflow rate × air specific heat × temperature". For the calorific calibration test, a non-metallic quartz glass container of the same shape, 400 mm long, 100 mm in diameter, and 1200 g in weight, was used.

Fig. 9 shows the measurement system for calorific value, neutron energy, neutron count, and electromotive force. The power supply for the ceramic heater that heats the container is connected to the container, and the neutron and electromotive force measurement equipment is installed next to the calorific value measurement box. For neutron count measurement, in addition to the NE213, an Aloka neutron Rem counter and a ^{3}He proportional counter, model TPS451C, were used. The measurement energy range is 0.025 eV to 15 MeV, the effective measurement range is 0.10 μSv/h to 10.0 mSv/h, and the neutron sensitivity is 1.3 cps/μSv h^{-1} ±10% (relative to the ^{252}Cf neutron beam). The instrument is installed 300 mm from the center of the instrument body, and signals are sent to a logger from the output terminal. Neutron calibration was performed using 96.5 mCi ^{252}Cf (April 15, 1985). The source half-life is 2.65 years, resulting in a strength of 3.05×10^{-5}. Based on the initial source strength, the neutron count as of January 2025 is calculated as $96.5 \times 10^{-3} \times 3.7 \times 10^7 \times 3.0 \times 10^{-5} = 1.071 \times 10^3 \times 10^{-3} \times 10^7 \times 10^{-5} = 1.071 \times 10^2$/s.

In other words, 107 neutrons are emitted from the source per second. Neutron energy measurements are described in [1]. All data is input to a Graphtec GL840 logger. The input impedance is 1 MΩ.

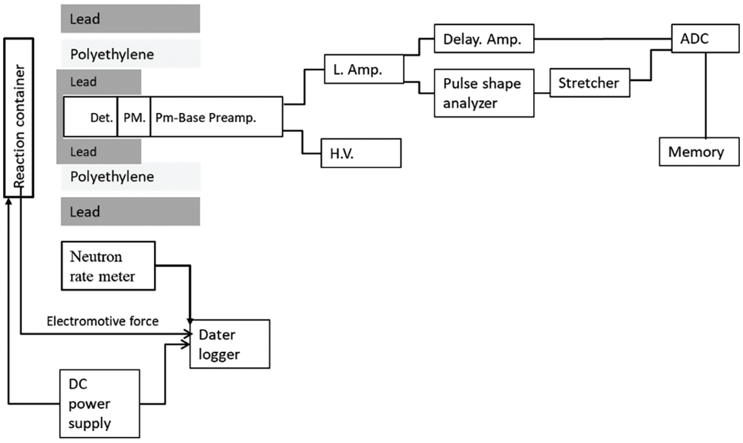

Fig. 9. Measurement system diagram.

3. EXPERIMENTAL RESULTS

3.1. *Calorie Measurement Results*

To calculate the energy generated by hydrogen's chemical reaction, compare the heat output of the reaction chamber with the heat output of chemical combustion if the chamber were filled with hydrogen at 1 atmosphere pressure. The combustion equation for hydrogen (H_2) is:

$$2H_2 + O_2 = 2H_2O + 284\ \text{kJ} \tag{4}$$

If 100 W of excess heat is continuously generated by the hydrogen oxidation reaction at 1 atmosphere pressure, the volume of hydrogen in the container is 100 mm in inner diameter and 400 mm in length, so its volume is 3142 cm^3. This is a 0.28 M H_2 content, so the total heat output is 0.28×284 kJ = 79.6 kJ. Therefore, the duration of 100 W of heat generation is calculated as $79.6 \times 10^3/100 = 796$ seconds. From the experimental results, typical values for excess heat at 26 W are $W_{ex} = 173$ kJ, at 44 W $W_{ex} = 2167$ kJ, and at 55 W $W_{ex} = 4780$ kJ.

The actual container pressure was 10 Pa, almost a vacuum, which is four orders of magnitude smaller than the assumed pressure of 0.1 MPa. Therefore, the heat generation amount assuming hydrogen at 1 atmosphere is 7.96 J, and the heat generation duration of 796 seconds is 0.08 seconds, which is a negligible value. The actual heat generation amount is more than six orders of magnitude greater than the assumed chemical combustion of hydrogen.

3.2. *Neutron, Electric Potential, and Electromagnetic Wave Measurement Results*

3.2.1. *Results in the Temperature Equilibrium Region*

Table I shows the results of experiments conducted under different test conditions, materials and processing conditions, gases, surface treatments, and temperatures. The table shows the detailed measurement results for input intensity, container temperature, presence or absence of excess heat, and neutron generation intensity. All values are from the thermal equilibrium region where the temperature is stable. The neutron values show the difference between the stable value at high temperature in the chamber and the background (BG) value of the calibration container with no input. The red color in the figure indicates that a statistically significant difference was observed.

The first column lists the container and sample materials, with representative examples including aluminum, titanium, steel, stainless steel 316 and 304, and finally Pyrex glass. The container shape is also described, with tests performed using closed-end pipes, foil, or plates packed into the calibration container.

The second column lists the internal gases, with hydrogen (99.995%) and deuterium (99.95%) gases used. Hydrogen pressures ranged from 2 Pa to 1 atmosphere. Deuterium gas pressures ranged from 2 to 5,000 Pa.

The third column lists surface treatments: electrolytic polishing to a mirror finish, or commercially available materials polished to 400# to 2,000# on both the inside and outside. A container with a high-temperature oxidized surface was used as the stainless-steel sample. This container, which had generated excess heat, was subjected to a high-temperature oxidation treatment in air at 800°C for approximately 24 hours. A container that did not generate heat was used with calibration specimens, foil, or plates.

The fourth column lists the heat input, which varies depending on the material.

TABLE I: Materials, Gases, Test Temperatures, Surface Finish, Power Input, Temperature, Output/input Power Ratio, Number of Tests, and Neutron Detection

Material	Gas	Surface polishing	Input watt	Temperature	Out/In ratio	Number of tests	Neutron emission
Al pipe; both ends closed	H_2:2Pa∼1atm	Electro, Emery	50∼300	50°C∼500°C	0.8∼0.9	5	Not detected
Al; both ends closed	D_2:2Pa∼5kPa	Electro, Emery	50∼300	50°C∼500°C	0.85∼0.95	15	Not examined
Al; foil and plate	H_2:2Pa∼1atm	Electro, Emery	50∼300	300°C∼500°C	0.8∼0.9	0	Not examined
Ti pipe; both ends closed	H_2:2Pa∼1atm	Electro, Emery	50∼600	50°C∼500°C	1.1∼1.2	5	Positive
Ti pipe; both ends closed	D_2:2Pa∼5kPa	Electro, Emery	50∼600	50°C∼500°C	1.11∼1.3	9	Positive
Ti; foil and plate	H_2:2Pa∼1atm	Electro, Emery	50∼600	50°C∼500°C	0.95∼1.0	18	Not examined
Steel pipe; both ends closed	H_2:2Pa∼1atm	Electro, Emery	50∼600	50°C∼600°C	0.94∼0.98	4	Positive
Steel pipe; both ends closed	D_2:2Pa∼5kPa	Electro, Emery	50∼600	50°C∼600°C	0.9∼0.97	4	Not examined
Steel; foil and plate	H_2:2Pa∼1atm	Electro, Emery	50∼600	50°C∼500°C	0.95∼0.98	0	Not examined
SUS 316 pipe; both ends closed	H_2:2Pa∼1atm	Electro, Emery	50∼600	50°C∼800°C	1.02∼1.5	37	Positive
SUS 316 pipe; both ends closed	D_2:2Pa∼5kPa	Electro, Emery	50∼600	50°C∼800°C	1.2∼1.6	88	Positive
SUS316; foil and plate	D_2:2Pa∼5kPa	Oxidized Surface	50∼600	700°C	0.9∼1.02	24	Not examined
SUS 304 pipe; both ends closed	H_2:2Pa∼1atm	Electro, Emery	50∼700	50°C∼800°C	1.2∼1.5	325	Positive
SUS 304 pipe; both ends closed	D_2:2Pa∼5kPa	Electro, Emery	50∼600	50°C∼800°C	1.2∼1.5	186	Positive
SUS 304 pipe; both ends closed	D_2:2Pa∼5kPa	Oxidized Surface	50∼600	50°C∼800°C	1.01∼1.02	2	Positive
SUS304; foil and plate	H_2:2Pa∼1atm	Electro, Emery	50∼600	50°C∼800°C	0.95∼1.01	53	Positive
SiO_2 Glass	H_2:2Pa∼1atm		50∼600	10°C∼700°C	0.8∼0.85	12	Not detected

The fifth column indicates the test temperature range. Measurements are typically conducted starting from 50°C, increasing the temperature in 50°C increments until the specified temperature is reached. A typical measurement lasts approximately 24 hours. At temperatures below 300°C, measurements can be conducted for as long as a week.

The sixth column indicates the resulting output/input ratio. Overall, the excess heat is lower than in the transpiration measurements. This is thought to be because the container temperature does not rise because air cools and removes heat directly from the container, resulting in less excess heat.

The values obtained using the thermal test method show that aluminum, steel, glass, and oxidized surfaces all yield values below 1. Ultimately, stainless steel materials were selected as representative containers for excess heat measurements. Titanium is also a promising candidate, but was not selected for testing due to its price.

The seventh column indicates the number of tests conducted. Since the exact number of tests is complex, this column shows an approximate number of tests conducted purely under the stated conditions. This represents more than 10 years of testing, with a total of over 3,000 tests. This table does not include electron irradiation of material surfaces or tests using various mixed metals. It lists the test conditions, surface treatments, and material test results after excess heat was confirmed.

Column 8 shows the neutron results. Tests written in red produced positive results. Neutrons were detected in all materials except aluminum and glass. No excess heat was detected in steel, but weak neutrons were. Neutrons were also detected in titanium.

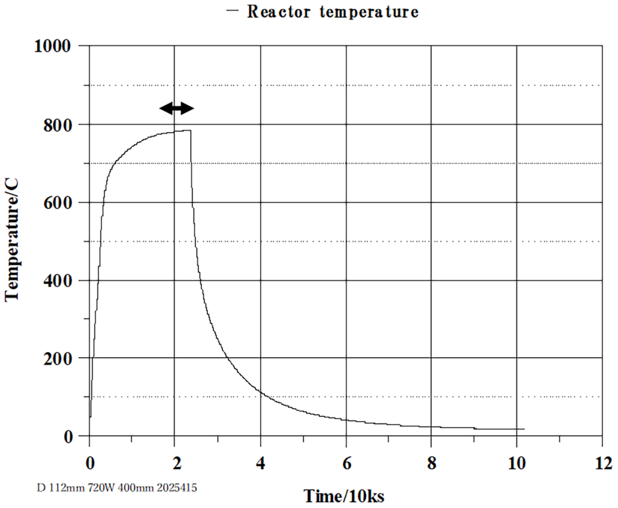

Fig. 10. Temperature change when input is 720 W.

Furthermore, no significant neutron detection was observed in plate or foil, even with stainless steel. There was no difference between hydrogen and deuterium gases. Importantly, all the SUS neutron detections were from cylindrically shaped containers.

We began testing the metal-gas system around 2011. For the first 10 years, we were unable to confirm excess heat, nor could we reproduce the generation of neutrons or electromotive force. The tests presented here focused on materials that generate heat, as summarized in Table I. We varied the reaction sample, container geometry, gas, input, pressure, and other factors. We investigated which combination of conditions was most likely to generate excess heat. Because we assumed this reaction was a nuclear reaction, we also focused on neutron detection. Initially, the necessary conditions for neutron generation were unclear, and although we also conducted tests using deuterium gas, no clear causal or correlational relationship was established. The correlation and causal relationship between temperature, excess heat, and other factors and neutrons remained unclear.

However, as shown in Table I, it became clear that heat was generated particularly from stainless steel systems. At one time, a stainless-steel cylindrical container was used for calibration, and the excess heat in the test container was sometimes lower than that in the calibration container. Subtracting the calibration data from the test container often resulted in a negative result. Initially, we suspected that an endothermic reaction might occur in the nuclear reaction. However, endothermic reactions are extremely unlikely. If such a reaction were to occur, it would mean that heat was converted into mass, rather than mass being converted into energy. To confirm this, we would need to examine the products, but this is extremely unlikely. Upon closer inspection, we discovered that the container itself could be reacting.

The stainless steel is 78% Fe, 18% chromium, and 8% nickel. Nickel is highly reactive to hydrogen, which could have emitted heat and neutrons.

Electrons and ions emitted from the container are collected by electrodes and output directly to a data logger as a voltage. Neutrons are also generated by the container, and their energy distribution and number are measured directly from the pulses outside the measurement box 80 cm away. Excess heat is measured using the air flow method, which allows for correlation with all measurement parameters.

We will explain the relationship between excess heat, neutrons, electromotive force, etc. using representative examples of test results. Fig. 10 shows the behavior of the container temperature when the input is 720 W. The container temperature reaches 780°C in about 20 ks, 5 hours. If the input is turned off at 25 ks, it will drop to room temperature in about 100 ks. Analysis at temperature equilibrium will be performed in the range indicated by the arrows in Fig. 10, from 18 to 22 ks, where the temperature becomes constant. However, clear results will not be obtained for subsequent phenomena such as neutrons and electromotive force even if they are performed in this stable temperature region.

Fig. 11 is a close-up of the output, input, net output, and chamber temperature for the first 20 ks in Fig. 10. From top to bottom, the figures show total output energy, input energy, temperature, and net (total output - input) output energy = excess energy.

The chamber temperature is gradually increased, with the total excess heat (red) reaching about 1.6 kW at about 3 ks. The net excess heat also reaches about 0.2 kW at 2 ks. The input power ultimately reaches 720 W. The furnace temperature (black) rises to 750°C at 20 ks.

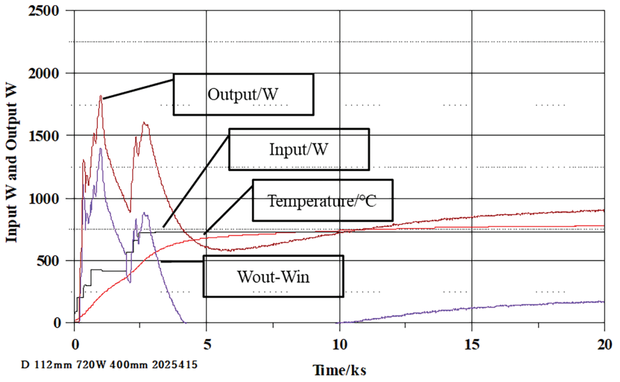

Fig. 11. The first 20 ks of Fig. 10.

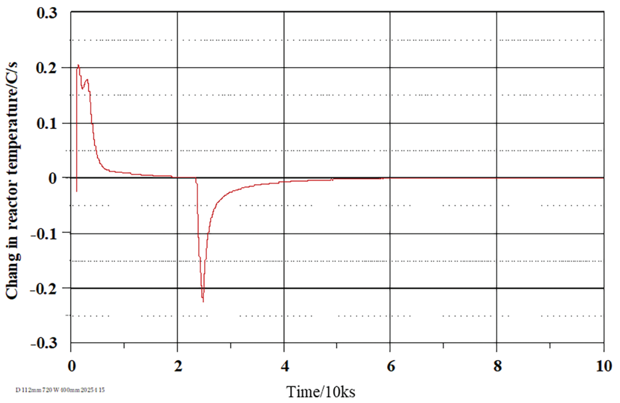

Fig. 12. Furnace temperature change rate (°C/s) for 100 ks in Fig. 10.

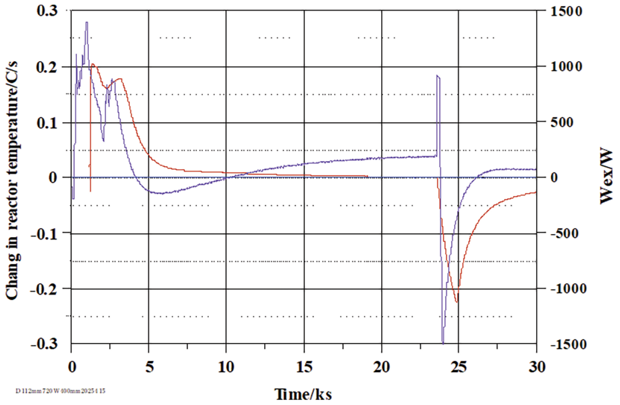

Fig. 13. Changes in container temperature change rate and excess heat generation.

Until now, neutron generation and electromotive force have been calculated in correlation with excess heat and furnace temperature, but by re-analyzing the temperature change rate of the stainless-steel container, the causal relationship can be clearly explained. Fig. 12 shows the furnace temperature change rate (°C/s) as a red line. The vertical axis shows the temperature change (°C/s), and in this case it reached a maximum of 0.2°C/s. If the input is stopped at 25 ks and the furnace temperature is lowered, the temporary temperature change rate drops to −0.22°C/s.

In Fig. 13, the temperature change rate (purple line: left vertical axis) and the excess heat from the furnace body (red line: right vertical axis) show similar fluctuations, as expected. This figure shows the fluctuations over the initial 30 ks of input. The excess heat calculation includes the furnace body temperature change, so the fluctuations are very similar. The excess heat generation (red line) occurs 0.5 ks after the temperature change (purple line). This indicates that the temperature change occurs first, followed by the excess heat generation. Currently, the maximum total heat generation is approximately 1.8 kW, which is approximately 2.5 times the thermal energy of the input of 720 W. As the temperature decreases, heat is absorbed by the container, and the minimum value is minus 1.5 kW.

Fig. 14 shows the relationship between container temperature change rate and neutron generation. It shows a clear causal relationship. Neutron generation is clearly caused by container temperature

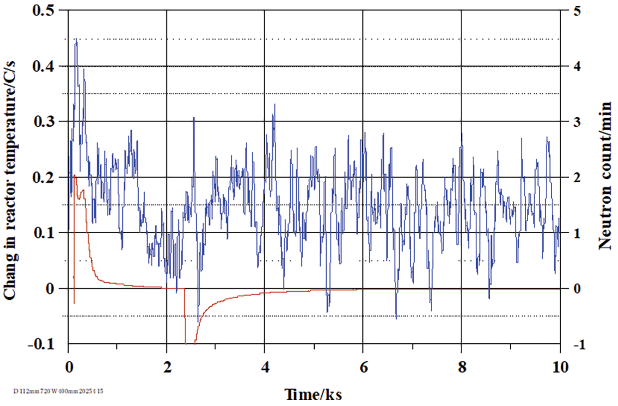

Fig. 14. Changes in container temperature change rate and neutron generation over 100 ks.

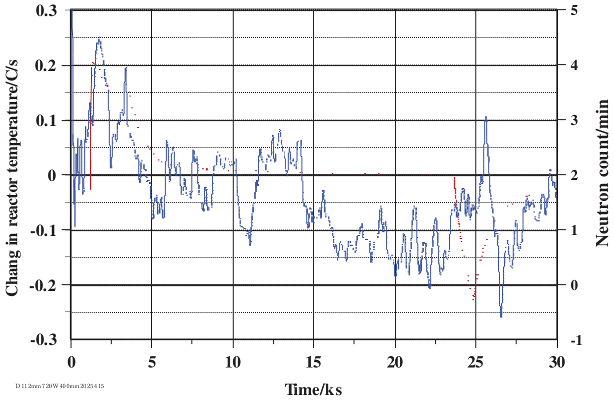

Fig. 15. Changes in the initial 30 ks of input in Fig. 14.

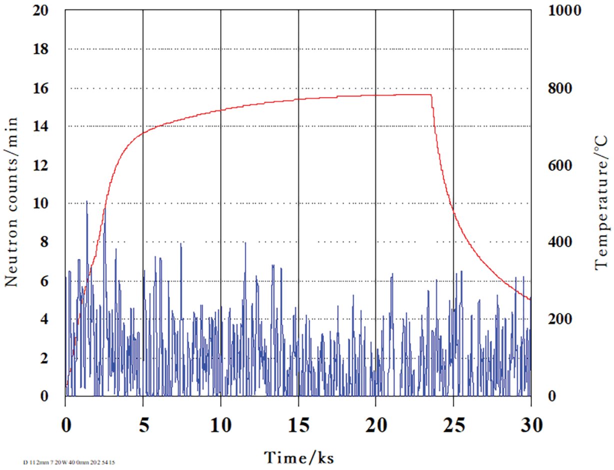

Fig. 16. Container temperature (right vertical axis, red line) and neutron generation (left vertical axis, blue line).

change, not temperature or excess heat generation. This phenomenon also shows a correlation over a wide range of temperature change rates.

Fig. 15 is an enlargement of Fig. 14, showing the causal relationship between the rate of temperature change (left vertical axis, red line) and neutron counts (right vertical axis, blue line) over the initial 30 ks of input. The vertical axes have been shifted so that the relationship between the two can be seen. The number of neutrons generated clearly shows a clear causal relationship with the container temperature change. It is notable that there is no delay from the temperature change due to excess heat generation as shown in Fig. 13, and neutron generation occurs immediately after the temperature change.

Fig. 16 plots the temperature of the container (red line on the right vertical axis) and neutron generation (blue line on the left vertical axis), but unlike Figs. 14 and 15, it shows that temperature has absolutely no relationship to neutron generation. In other words, it is not simply temperature, but temperature changes that trigger neutron generation.

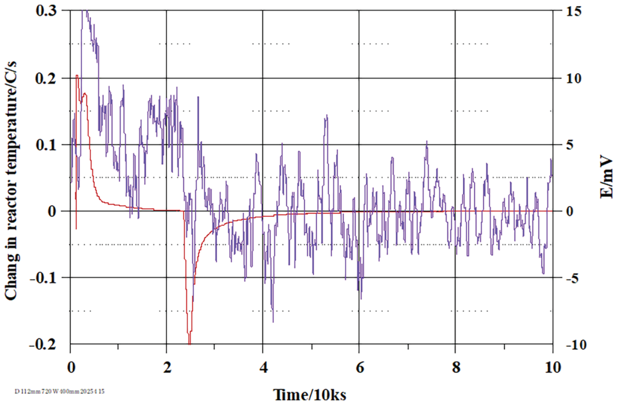

Fig. 17. Change in furnace temperature and electromotive force.

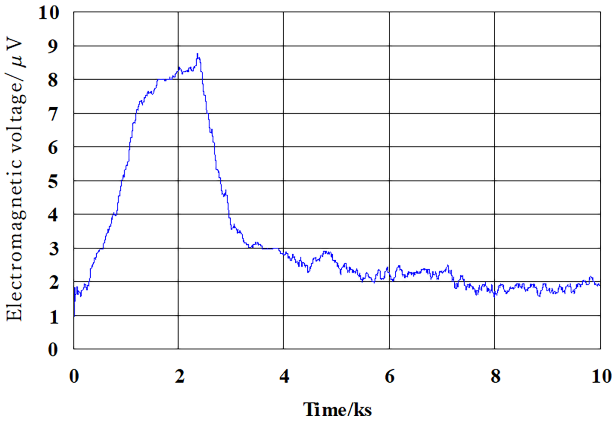

Fig. 18. Changes in electromagnetic radiation over 100 ks.

Fig. 17 shows the causal relationship between the rate of change of container temperature and the change in electromotive force. The purple line (right vertical axis) represents the electromotive force, and shows its causal relationship with the rate of change of container temperature (red line: left vertical axis). Unlike neutron generation (Figs. 14 and 15), electromotive force is generated even when the temperature change is small around 20 ks.

The fact that electromotive force is generated even when the container temperature drops suggests that the generation of electromotive force is affected by both the container surface temperature and the rate of temperature change. Furthermore, the behavior is like that of neutrons in Figs. 14 and 15; when there is a temperature change, a reaction occurs, although with a time delay of several hundred seconds. Furthermore, even when there is no temperature change, electromotive force is generated between 15 and 25 ks. In this case, too, the generation of electromotive force is triggered by temperature change.

Fig. 18 shows the electromagnetic radiation for 100 ks, and clearly shows a strong correlation with the container temperature in Fig. 10. In this case, the temperature change is not the trigger.

Table II shows, from left to right, the date, input (W), container temperature (°C), excess energy (W) during the measurement period, electromotive force (mV), electromagnetic waves (mG), neutron generation (nSv/h), input (J), output (J), output/input ratio, and excess energy per container area (W/cm^2). Red text in the figure indicates values below the background value (BG), i.e., negative values. All calculations are test values in the temperature equilibrium region when the temperature is stable.

Fig. 19 shows an approximation of the relationship between temperature change rate and excess heat, obtained using approximately 20,000 measured values from the test in Fig. 10. While there is some variation in the graph, it can be expressed as a roughly exponential function. The correlation coefficient between temperature change rate and excess heat is around 0.4, and can be expressed as a simple exponential function.

Similarly, the neutron generation in Fig. 20 is expressed as an exponential function, and increases rapidly as the temperature changes. Here, the neutron generation rate is calculated in direct the data.

The relationship between electromotive force and temperature change rate in Fig. 21 can also be expressed as an exponential approximation, and Fig. 21 shows a rapid increase in the temperature change rate.

TABLE II: Measurement results of neutrons, electromotive force, and electromagnetic waves from November 2024 to April 2025

	Input W	Reactor Temp.	Excess Watt	Electro-motive voltage	Electro-motive force	Neutron	Input Joule	Output Joule	Out/In	Hex Joule	W/cm^2
YMD	W	°C	W	mV	mG	nSv/h	J	J		J	W/cm^2
20241125	724.7	783.1	228.8	6.664	**(0.00022)**	0.864	3.282E + 06	5.569E + 06	1.697	2.29E + 06	0.229
20241129	724.2	763.8	441.9	7.372	0.00048	1.064	1.712E + 06	3.922E + 06	2.29	2.21E + 06	0.442
20241114	216.9	403.3	87.0	10.171	0.00107	1.756	9.389E + 06	1.156E + 07	1.232	2.18E + 06	0.087
20201129	724.2	763.8	193.7	22.545	0.00248	0.803	3.657E + 05	4.626E + 05	1.265	9.69E + 04	0.194
20241021	583.8	726.9	97.3	22.545	0.00248	0.803	1.629E + 07	1.896E + 07	1.164	2.68E + 06	0.097
20241029	698.9	782.6	120.0	3.273	0.00148	1.972	1.751E + 06	2.051E + 06	1.171	3.00E + 05	0.120
20241120	720.0	622.0	460.2	14.586	0.00128	1.554	2.093E + 06	3.474E + 06	1.659	1.38E + 06	0.460
20241119	547.0	561.9	294.3	13.951	0.00134	**(1.043)**	2.697E + 06	4.168E + 06	1.546	1.47E + 06	0.294
20240805	478.4	589.0	122.4	1.507	**(0.00079)**	0.415	2.359E + 06	8.316E + 06	1.202	5.96E + 06	0.122
20250414	536.274	377.328	1010.564	11.568	**(0.00071)**	2.083	2630422	4956818	1.884	2.33E + 06	2.326
20250415	307.347	202.831	770.667	3.908	**(0.00033)**	0.670	1461433	3664520	2.507	2.20E + 03	2.203
Back ground	0.0	25.0	0.0	0.186	0.00152	1.4299	–	–	–	–	–

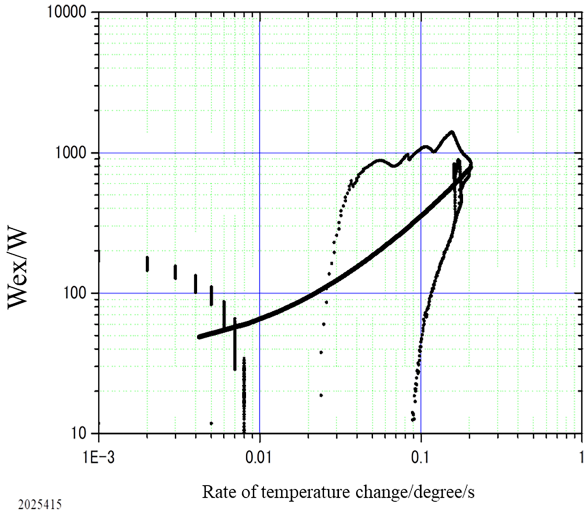

Fig. 19. Relationship between furnace temperature change rate and excess heat expressed as an approximation formula for 20,000 measurement points.

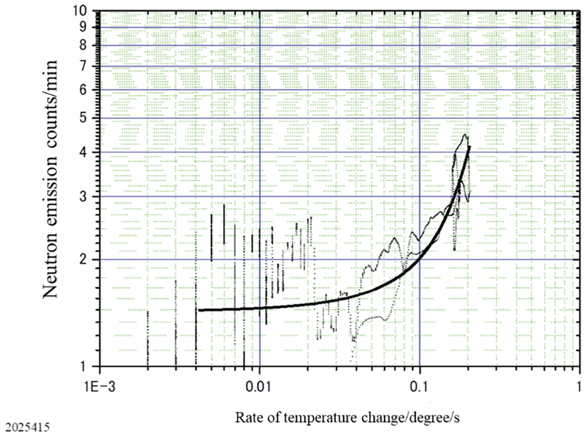

Fig. 20. Relationship between container temperature change rate and neutron generation, expressed as an approximation for 20,000 measurement points in the Fig. 10 test.

Fig. 22 shows the changes in excess heat, neutrons, and electromotive force on a single graph. The horizontal axis shows the temperature change rate up to 2°C/s. Experimental values range from 0.2 to 0.3°C/s, but the graph shows an approximate change up to 2°C/s. Here, the vertical axis is logarithmic and the horizontal axis is linear. Actual tests were conducted only up to a change rate of 0.2°C/s; temperature change rates above that are calculated values. Therefore, it is unclear what results would be obtained using actual temperature change rates.

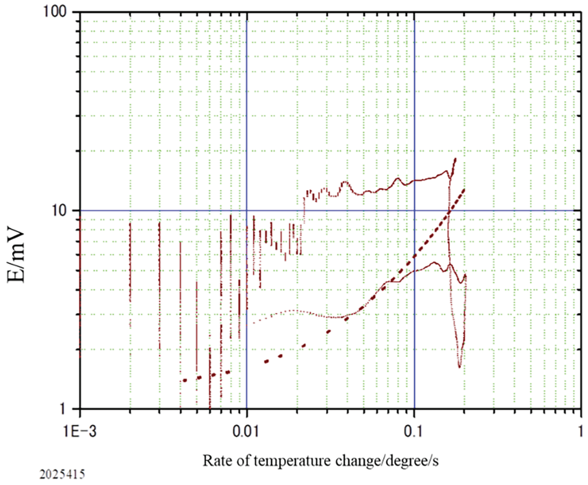

Fig. 21. Relationship between container temperature change rate and electromotive force generation, expressed as an approximate equation for 20,000 measurement points in Fig. 12.

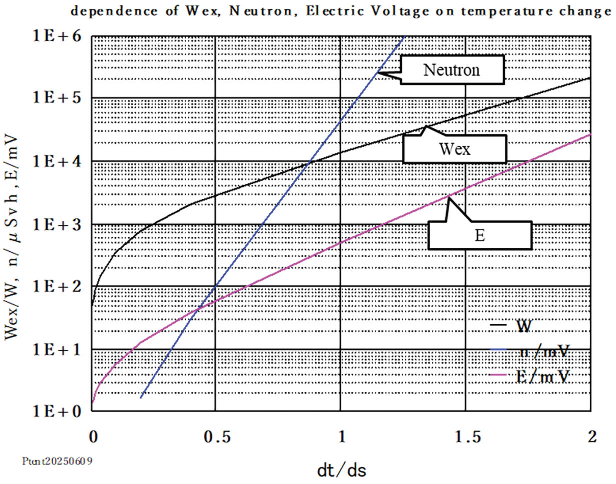

Fig. 22. Excess heat, neutrons, and electromotive force changes calculated using an exponential approximation formula, with a temperature change rate up to 2°C/s.

4. Discussion and Conclusions

We believe that the generation of neutrons and electromotive force occurs through interactions with hydrogen atoms on the surface and inside of the container. This phenomenon occurs not in the temperature equilibrium region but in the non-equilibrium region. This clearly indicates a strong causal relationship between neutron and electromotive force generation and changes in container temperature. Furthermore, electromagnetic wave generation is caused by the container temperature. We hypothesize that temperature differences in various parts of the container change the movement speed of hydrogen or other reactants, thereby driving the reactions that generate excess heat, neutrons, and electromotive force.

Fig. 22 shows the results of calculations with temperature change rates up to 2°C/s. The increases in excess heat (black line) and electromotive force (purple line) show similar trends. Neutrons (blue line) rise more rapidly.

This reveals an important point. While experimental temperature change rates of up to 0.2°C/s have been obtained, we believe that it is possible to artificially control conditions to induce temperature changes of more than 2°C/s and achieve strong reactions.

Next, the test results show that, assuming a typical excess heat generation rate of 1 W/cm^2 per unit area of reactant, and assuming an estimated nuclear reaction rate of 1 MeV/reaction, the number of hydrogen atoms consumed would be approximately $10^{12}/cm^2/s$. The measured dissolved hydrogen concentration in the manufactured stainless steel was reported to be 1×10^{20} H $atoms/cm^3$ [13].

This value, calculated per area, approximates 10^{12} H/cm^2. Because there are sufficient hydrogen atoms present within the metal, calculations suggest that there will be no shortage of raw hydrogen for 10^8 seconds, allowing the reaction to continue for more than three years. Furthermore, in addition to the hydrogen originally present in the metal, large amounts of H_2O are also present in vacuum and the atmosphere. Ōmi et al. [14] have reported that hydrogen radicals are generated from the H_2O present on heated nickel and SUS surfaces. The reaction can continue if this hydrogen is supplied as a reactant.

Furthermore, electron-emitting reactions occur during the reaction. At 0.1°C/s, 10^{10} electrons are emitted per mole of atom per second. Assuming $e = 1.602 \times 10^{-19}$ coulombs, this corresponds to an electrical charge of 1.6×10^{-9} C/s. Calculating from the logger's 1 MΩ input impedance, this yields 1.6 nA.

When stress is applied, the crystal structure changes; the BCC structure has more voids than the FCC structure, making hydrogen more likely to diffuse. Furthermore, stress also increases internal defects. The SUS container body is heated by a heater, reaching a maximum temperature of approximately 800°C. Hydrogen migrates depending on its mobility, solubility, concentration, and temperature gradient. Extensive research has been conducted on these factors, and analysis is possible using published data.

We estimate the migration and reactions of hydrogen in SUS. The analysis is performed in the stable equilibrium region, but more accurately, it should be performed in the non-equilibrium region. SUS304 has an austenitic structure (FCC crystal gamma phase) and a face-centered cubic crystal system. When stainless steel is subjected to stress, its structure changes to martensite (BCC crystal α' phase). In this structure, hydrogen mobility increases by approximately five to six orders of magnitude. This results in higher hydrogen mobility with respect to temperature changes than in its original state.

Even in a vacuum, a large amount of H_2O is present in the chamber. H_2O in the container is adsorbed onto the walls and becomes hydrogen molecules. These molecules become atomic hydrogen on the SUS surface, which is free of impurities and oxides. They then react with the metal, absorbing electrons and becoming extremely small protons, or hydrogen nuclei. Protons have high diffusion rates and reactivity in metals.

When there is a temperature difference in the stainless steel, protons will move from the hotter area to the colder area if the proton concentration in the metal is the same. The container used in this experiment was heated using a ceramic heater. Changing the power input on or inside the container results in temperature differences within and on the surface of the metal. The greater the power input change, the longer it takes for the temperature to reach equilibrium. Over time, the temperature and hydrogen concentration distributions disappear and become uniform. In SUS, it is predicted that new reaction sites will increase due to processing and other factors. In addition, the protons that are originally present are distributed stably in the O site (octahedral position) and T site (tetrahedral position), but are also affected by temperature changes and processing. From this point on, it is assumed that protons simultaneously enter the reaction site, and a reaction occurs depending on the temperature and concentration. In terms of the reaction mechanism, there is also a theory that this reaction occurs due to quantum effects.

ACKNOWLEDGMENT

We would like to express our sincere gratitude to the following people for their financial support in continuing our research and development: Ms. Sanae Numata (wife of the late Dr. Hiroo Numata), Mr. Mitsugu Sasaki (CS Tokki), and Ms. Fujiko Usui.

CONFLICT OF INTEREST

The authors declare that they have no conflicts of interest.

REFERENCES

[1] Mizuno T. Neutrons produced by heating processed metals. *Eur J Appl Phys*. 2025;7(4):3–18.

[2] Mizuno T, Akimoto T, Sato N. Neutron evolution from annealed palladium cathode in LiOD-D_2O solution. *Electrochem Ind Phys Chem*. 1989;57(7):742–3.

[3] Mizuno T, Ohmori T, Enyo M. Isotopic changes of the reaction products induced by cathodic electrolysis in Pd. *J New Energy*. 1996;1(3):31–47.

[4] Mizuno T, Ohmori T, Kurokawa K, Akimoto T, Kitaichi M, Inoda K, *et al.* Anomalous isotopic distribution of elements deposited on palladium induced by cathodic electrolysis. *Denki Kagaku*. 1996;64(11):1160–5. [in Japanese].

[5] Mizuno T, Ohmori T, Akimoto T, Kurokawa K, Kitaichi M, Inoda K, *et al.* Isotopic distribution for the elements evolved in palladium cathode after electrolysis in D_2O solution. *Prog New Hydrog Energy*. 1996;2:665–9.

[6] Mizuno T, Ohmori T, Enyo M. Confirmation of the changes of isotopic distribution for the elements on palladium cathode after strong electrolysis in D_2O solution. *Int J Soc Mater Eng Resour*. 1998;1:45–59.

[7] Ohmori T, Mizuno T, Kurokawa K, Enyo M. Nuclear transmutation reaction occurring during the light water electrolysis on Pd electrode. *Int J Soc Mater Eng Resour*. 1998;1:35–44.

[8] Alabin KA, Andreev SN, Sobolev AG, Zabavin SN, Parkhomov AG, Timerbulatov TR. Isotopic and elemental composition of substance in nickel-hydrogen heat generators. *J Condensed Matter Nucl Sci*. 2018;26:32–44.

[9] Beiting EJ, Romein D. High-temperature calorimetric measurements of heat for Ni/H2 exothermic reactions. *J Condensed Matter Nucl Sci*. 2019;29:41–51.
[10] Mizuno T, Rothwell J. Anomalous heat reaction from hydrogen and metals. *J Condens Matter Nucl Sci*. 2025;39:417–36.
[11] Itagaki A, Murase Y, Tosa M, Suzuki S, Takagi S, Gotoh T. Effect of surface processing on hydrogen desorption from stainless steel to UHV. *J Vac Soc Jpn*. 2014;57(1):23–6.
[12] Ishimaru E, Hamasaki H, Ohno T, Yoshida F. Stress-strain behavior and microstructure change of type 304 stainless steel under tension and compression. *J Jpn Soc Technol Plast*. 2014;55(642):33–7.
[13] Hagi H, Yanagawa T. Analysis of hydrogen in cathodically polarized austenitic stainless steels. *Fukui Univ Technol Res Bull*. 2017;37:109–16.
[14] Ōmi T, editor. *Product Innovation Opened by Gas Science*. Tokyo: Realize Co., Ltd.; 1996 Jan 31. Chapter 2, Materials, surface treatment, and welding for trouble-free performance; p. 160–79.